Numerical Simulations of a Landing Gear with Flow Through Fairings for Noise Mitigation

AIAA AVIATION Forum
12-16 June 2023, San Diego, CA and Online
AIAA AVIATION 2023 Forum

10.2514/6.2023-4173

Numerical Simulations of a Landing Gear with Flow Through Fairings for Noise Mitigation

Marc Terracol* and Lucas Manueco†
ONERA, DAAA, Université de Paris-Saclay, F-92190, Meudon, FRANCE.

Eric Manoha‡
ONERA, DAAA, Université de Paris-Saclay, F-92322, Châtillon, FRANCE.

Francesco Avallone§, Daniele Ragni¶ and Alejandro Rubio Carpio‖
Faculty of Aerospace Engineering, Delft University of Technology, Kluyverweg 1, 2629 HS Delft, The Netherlands

This study presents a numerical investigation of the noise mitigation effect provided by several fairings placed upstream of a simplified two-wheel landing gear. The chosen configuration is equipped with detachable elements that mimic realistic components, *e.g.* brakes and torque link, to include representative landing gear noise sources. Several numerical simulations of the flow developing around this landing gear have been carried out, with or without an additional upstream fairing to control the noise generation processes. The chosen configurations match those from related experiments performed at the Delft University of Technology. Both the numerical and the experimental studies are conducted in the framework of the European Union Horizon 2020 research project INVENTOR (INnoVative dEsign of iNstalled airframe componenTs for aircraft nOise Reduction). The numerical method is based on the Zonal Detached Eddy Simulation approach, applied on a set of Cartesian octree grids with a specific immersed boundary wall treatment. Both solid and wire mesh fairings are considered, the latter being accounted for thanks to a specific wire mesh numerical model. Overall, the simulations show a nice agreement with the measurements and allow a thorough analysis of the flow modifications responsible for noise mitigation when the fairings are introduced.

Nomenclature

β	Wire mesh porosity coefficient
C_t	Modeling coefficient
d	Wire diameter, m
D	Wheel diameter, m
Δt	Time-step, s
Δv	Wire mesh deflection coefficient
Δx	Grid resolution, m
h	Aperture of the wire mesh, m
ν	Fluid kinematic viscosity, m^2/s
ν_t	Turbulent kinematic viscosity, m^2/s
μ	Fluid dynamic viscosity, kg/m/s
μ_t	Turbulent dynamic viscosity, kg/m/s
K	Pressure resistance coefficient
p	Pressure, Pa
ρ	Density, kg/m^3
Re_d	Reynolds number based on the wire diameter

*Dr, Department of Aerodynamics, Aeroelasticity and Acoustics, AIAA member. Marc.Terracol@onera.fr.
†Dr, Department of Aerodynamics, Aeroelasticity and Acoustics.
‡Dr, Department of Aerodynamics, Aeroelasticity and Acoustics, AIAA member.
§Assistant Professor, Delft University of Technology, AIAA member.
¶Associate Professor, Delft University of Technology, AIAA member.
‖Dr., Delft University of Technology.

u_i	Components of velocity ($i = 1, 2, 3$), m/s
u_n	Component of velocity normal to the wire mesh, m/s
u_t	Component of velocity tangential to the wall or wire mesh, m/s
u_τ	Friction velocity, m/s
U_∞	Free-stream velocity, m/s
u, v, w	Components of velocity in the respective x, y and z directions, m/s
x, y, z	Spatial coordinates, m

I. Introduction

Among the different airframe noise sources of modern airliners, the landing gears are generally considered as a prominent one, especially during approach and landing. The important noise generation due to the flow developing around the landing gears is due to the interaction of a complex separated flow of different components, that interacts with downstream parts and generates high-intensity broadband noise. Therefore, several passive control solutions have been developed in the past decades, leading to the introduction of dedicated fairings surrounding the landing gear elements. The main goal of such fairings, is to deflect the flow such that it does no longer interact directly with specific landing gear parts. Solid fairings usually provide good noise reduction properties, but often at the costs of a too large drag and installation penalty. Alternatively, porous fairings were demonstrated in several studies to yield significant noise reduction (e.g. [1–3]). These flow-through fairings may have significant benefits compared to solid ones, in terms of drag penalty, weight, brake cooling and bogie maintenance [3]. Most of the fairings considered in practice are usually made of perforated plates *e.g.* [4], but other alternative, such as wire meshes appear as a valuable option [5–8]. A dedicated program to study and categorize flow-through fairings for the mitigation of landing gear noise is currently under progress in the framework of the European Union Horizon 2020 research project INVENTOR (INnoVative dEsign of iNstalled airframe componenTs for aircraft nOise Reduction). A wide range of fairings is under investigation in this project, including perforated plates, wire meshes, metallic wool or diamond-lattice material [9], with several objectives: i/ to identify the most efficient flow-through materials for noise mitigation; ii/ to better understand the flow behavior around the landing gear when using flow-through fairings; iii/ to improve the capability of the numerical tools to properly simulate such devices. This point represents one of the main difficulties, since flow-through materials usually involve very small pores or open areas compared to the size of the landing gears. This makes their direct resolution almost impossible to perform, due to computational limitations, or at the expanse of large computational grids, *e.g.* [10]. Therefore, dedicated macroscopic numerical models have to be developed and validated.

This study focuses on the modeling and simulation of a simplified landing gear equipped with a fairing. It is based on a modified version of the LAGOON configuration [11], which has been extensively investigated in the framework of the BANC workshop series [12]. Although this configuration is simplified compared to an "in flight" landing gear, several key elements are included to be as representative as possible from a realistic configuration. More specifically, the torque-link and brake-like protuberances have been included during the tests and simulations. An important experimental campaign on this configuration has been performed at the Delft University of Technology (TUD) in the framework of the INVENTOR project. The results obtained during this campaign represent a valuable database to validate the numerical approaches used to simulate landing gear flows. In this paper, we present the application of a numerical wire mesh model, previously developed in [7] to the simulation of this experimental configuration. This model makes it possible to introduce wire mesh fairings in scale-resolving unsteady simulations using hybrid RANS/LES techniques (*e.g.* ZDES). Several configurations are simulated and compared to the experiments, including the baseline configuration without fairing, and three controlled configurations with a solid or wire mesh fairings. These simulations make it possible to investigate the flow modifications provided by each type of fairing and their respective performances on noise mitigation.

The paper is organized as follows: First, Section II presents the simplified landing gear configuration and the experimental setup at TUD. Then, Section III presents the numerical method. It relies on the use of the Zonal Detached Eddy Simulation (ZDES) approach, on a set of Cartesian octree grids. The method makes use of a wall model, which is detailed. This section also recalls the basis of the numerical wire mesh model developed in [7]. Section IV then presents the results obtained on the baseline configuration, with an extensive assessment of the simulation results against the measurements. The numerical method is then applied to the landing gear with fairing configuration in Section V. Three types of fairings are considered: a solid one and two wire meshes with different characteristics. Section VI presents a physical analysis of the flow patterns responsible for noise generation, as well as an insight into the flow modifications that possibly lead to noise mitigation. The acoustic performances of the various fairings are also evaluated by a far-field

noise prediction based on the solid FW-H approach. Finally, Section VII recaps the main conclusions from this study, as well as future works to be done.

II. Experimental setup and configurations

A. LAGOON-like Landing Gear model

The LAGOON landing gear was originally conceived in the 2000's to build an experimental database for the validation of CAA techniques for airframe noise applications[11]. The model represents a simplified version of a nose landing gear (NLG) or a direct main landing gear (MLG), and the baseline configuration consists of a profiled rod, a round main rod, a wheel axle and two wheels with inner rim cavities.

The present mock-up is a modified, downscaled version of the LAGOON model, hereafter referred to as "LAGOON-like LG". This model is scaled down to a wheel diameter of 15 cm (hence having a 1:5 scale with respect to a real NLG) in order to minimize blockage effects. The cylindrical cavities on the inner side of the wheels, that produced unrealistic tones due to the appearance of Rossiter-type feedback-loop instabilities in the original LAGOON model [13], are closed with flat covers. Additionally, the model is equipped with representative elements of an Airbus A320 MLG configuration such as a torque link allocated upstream the main rod, or brake-like protuberances (see Figure 1) to reproduce most of the noise sources mimicking a real configuration. Furthermore, the profiled rod section, that was originally included in the LAGOON LG to minimize noise scattering due to the interaction between the wind-tunnel jet shear layer and the LG cylindrical rod, is just a detachable cover in the present configuration and not included in the model for this study, *i.e.* only the cylindrical rod is exposed to the flow.

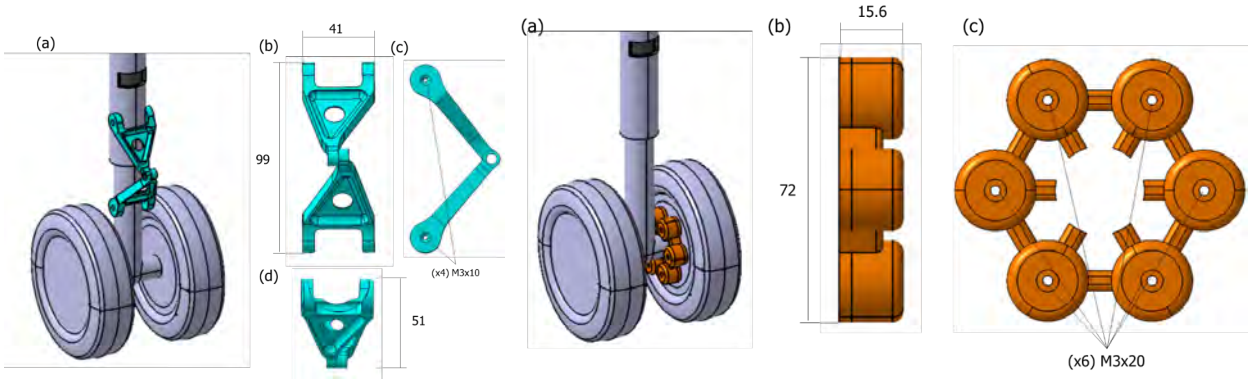

Fig. 1 LAGOON-like landing gear with Torque link (in light blue) or brake-like protuberances (in orange). Distances in mm. (a) Isometric view of assembly with baseline model (b) Front view (c) Side view (d) Top view.

The experiments have been conducted in the aeroacoustic vertical wind tunnel (A-Tunnel) at Delft University of Technology (TUD). The tunnel is an open-jet closed-circuit facility with the test section located in an anechoic plenum with dimensions $6.4 \times 6.4 \times 3.2$ m^3. The model is placed horizontally with the wheel axle at the center of the 40×70 cm^2 nozzle exit (Figure 2). The distance between axle and nozzle exit can be adapted to guarantee the localization of noise sources of interest. A flat plate is flush mounted to the nozzle exit to mimic the aircraft wing (or fuselage belly for NLG). The model is attached to the tunnel with a turntable, which allows to adjust the yaw angle. Overall, the A-tunnel exhibits good performance, in terms of flow uniformity and turbulence intensity (lower then 0.1%) and in terms of background noise levels, free-field propagation and reverberation time [14].

The model is also equipped with a mounting support for different types of solid or flow-permeable fairings (see Figure 3). The mounting support is attached directly to the LAGOON-like model through anchorage points at main rod and wheels. This configuration limits the presence of auxiliary struts (which might have a non-negligible effect on the resulting flow and acoustic fields), minimizes vibrations, and it mimics the support in a real configuration. The mounting support allows to install flat fairings with dimensions of 54 x 270 mm^2. The fairing covers wheel axle, brakes, torque link and the lower part of the main rod. The support allows to install solid and porous panels with thickness of up to 10 mm.

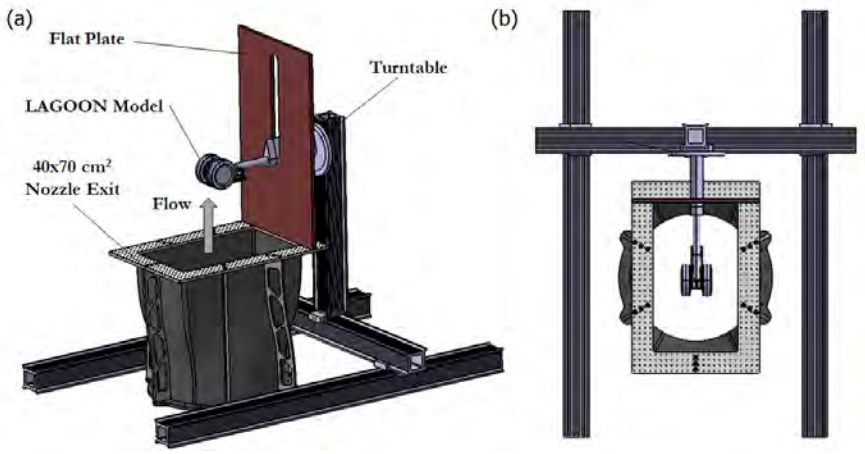

Fig. 2 Sketch of the experimental setup. (a) Isometric view (b) Top view.

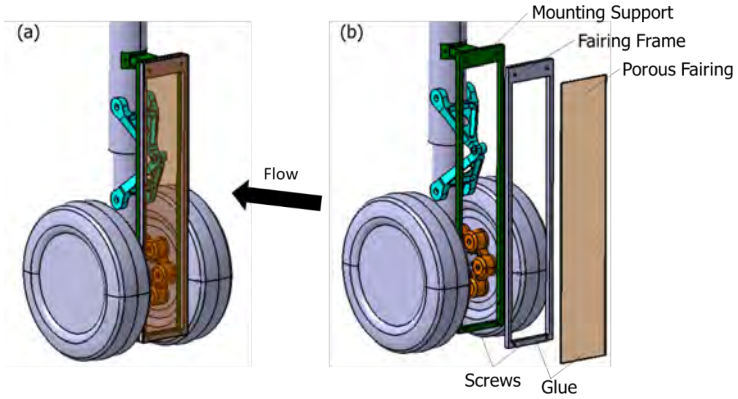

Fig. 3 Mounting support (green), fairing frame (grey) and porous fairings (orange, translucid) installed on the baseline LAGOON-like model. (a) Isometric view (b) Exploded schematic.

Fig. 4 Wire mesh samples considered in the study. Left: coarse wire mesh and fine wire mesh. Right: geometrical wire mesh parameters d and h.

Several kind of materials have been considered for the fairings, including solid and porous ones. Among the other tested porous fairings (perforated plates, diamond-lattice meta-materials, metallic wool), the present study will focus on the use of wire mesh fairings. Two different types of square-pattern wire meshes will be considered, with different sizes of the wires and aperture dimensions (see Figure 4):

1) The first one will be referred to as the coarse wire mesh and is defined by a wire diameter d = 1 mm and an opening size of h = 5 mm. Its porosity is $\beta = (1 - d/h)^2$ =0.64. These characteristics have been selected so that they match those from previous studies in the framework of the IMAGE project [7, 8]
2) The second one, proposed by DLR in the framework of the INVENTOR project, offers significantly more resistance to the flow and will be referred to as the fine wire mesh in the following. Its wire diameter is d = 0.042 mm and an opening size of h = 0.182 mm. Its porosity is β =0.59.

B. Flow Field Measurements

Static pressure data over the main rod and wheels are obtained by means of pressure taps. The number of taps is limited by the availability of space to host the cabling inside the model. Twenty pressure taps are allocated at the midspan plane of the left-side (as seen from the back of the model) wheel along the entire circumference, with steps of 18 degrees (Figure 5). The right wheel is instrumented with three pressure taps at locations 0, 1 and 19. These will be employed to assess the symmetry of the set-up. Moreover, 17 pressure taps are allocated in the main rod both axially and circumferentially. Axial taps are within 50 and 70 mm away from the axle axis, with steps of 5 mm. Circumferential taps are distributed over the streamwise-vertical plane located 50 mm away from the axle. Taps are distributed among both stagnation points with steps of 12 degrees. Taps at 72 and 84 degrees are not included due to manufacturing constraints.

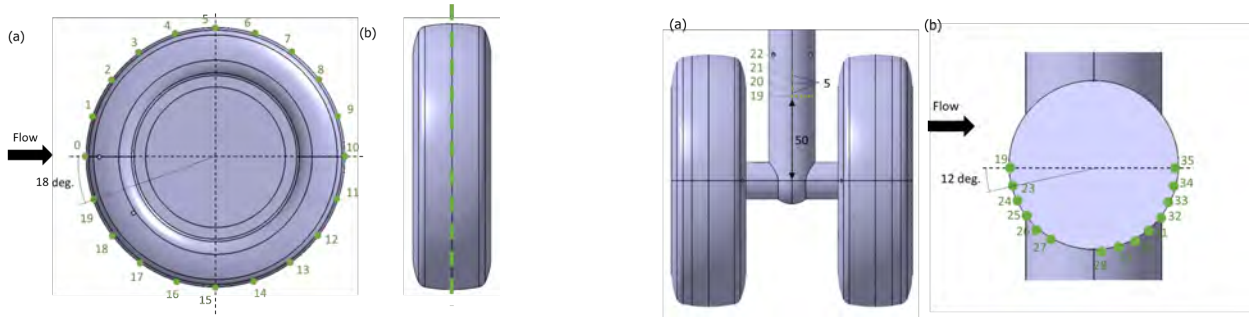

Fig. 5 Pressure taps distribution on the mock-up.

Finally, the wake flow is characterized with stereoscopic Particle Image Velocimetry (PIV) [15] on vertical-spanwise cross-sections, as well as a series of planar PIV measurements on different streamwise-spanwise planes (Figure 6).

C. Acoustic Measurements

Acoustic measurements are carried out with a 2 x 1 m^2 microphone antenna comprising 64 40PH G.R.A.S. microphones. The antenna is placed 1.5 meters away from the model, and data are obtained with the array in a “flyover" configuration, i.e. with the array looking at the bottom of the LAGOON-like LG. Additional measurements with the antenna looking from the side have also be performed on the configurations regarding the torque link. These setups allow to retrieve absolute far-field noise levels, as well as to localize and isolate noise generation at different regions within the model.

D. Flow conditions

Measurements have been performed at Mach numbers of 0.04, 0.07 and 0.1, corresponding to respective free-stream velocities of 15, 25 and 35 m/s. In the present study, only the highest velocity value will be considered, *i.e.* U_∞ = 35 m/s. The corresponding Reynolds number, based on the wheel diameter is $Re_D \simeq 350,000$.

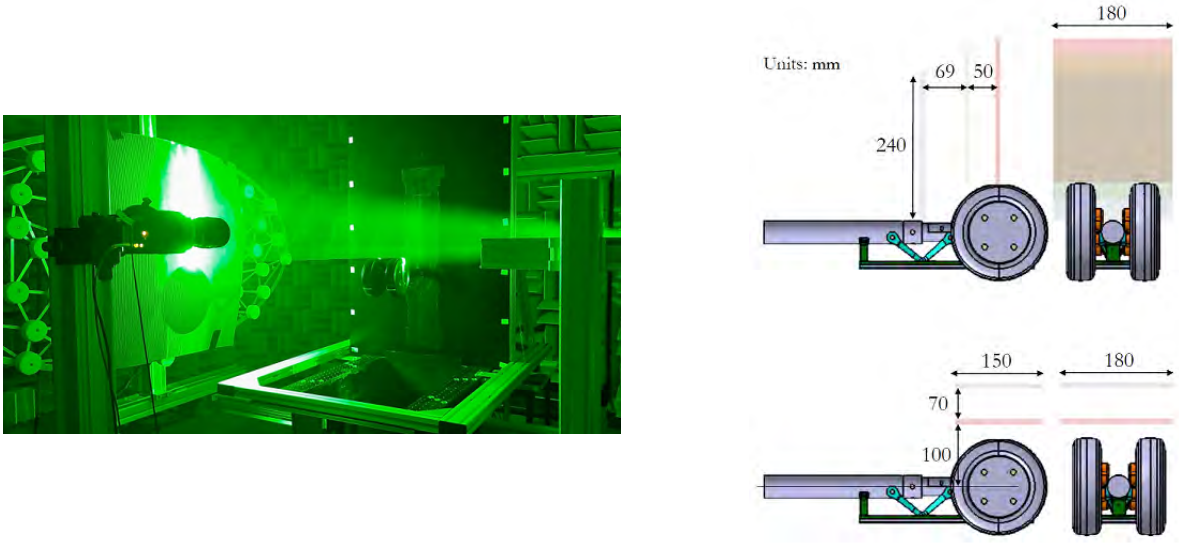

Fig. 6 PIV setup and measurement planes. Distances in mm.

III. Simulation approach

A. Numerical method

The simulations presented in this study have been carried out using ONERA's in-house research solver FUNk. This code resolves the compressible Navier-Stokes equations using a finite-volume formulation. Several strategies for turbulence resolution and modeling are available: RANS, ZDES, LES and DNS.

The numerical scheme used to perform the present simulations is the modified AUSM+(P) scheme [16] that minimizes the numerical dissipation by introducing a wiggle detector.

Time integration uses a second-order implicit backward-Euler scheme, which involves a Newton sub-iteration process at each time step.

The computations reported in Section IV and V are based on a hybrid RANS/LES approach: the ZDES mode 2 2020 [17]. This approach was demonstrated to be capable of ensuring an enhanced shielding of attached boundary layers in RANS mode, even on fine and/or isotropic grids (see [17] for details), while it stills allows for a rapid switch to LES mode in separated areas. The underlying turbulence model is the Spalart-Allmaras model [18].

All the simulations reported in this paper have been done using an Immersed Boundary Methodology, on Cartesian octree grids. These grids are generated quasi-automatically using ONERA's pre- and post-processing tool Cassiopee [19]. To avoid the use of too fine grid resolutions, wall models are used in the vicinity of solid surfaces (see next section). More details on the numerical method and the Immersed Boundary Method implementation can be found in [7].

B. Wall model

1. Turbulent boundary layers

The wall law proposed by Allmaras *et al.* [20] has been retained in this study for the velocity prediction near the wall. This law is an analytical solution of the equilibrium boundary layer equations, closed by the Spalart-Allmaras model, which makes it very consistent with the present numerical method based on the SA model. The analytical expression of the tangential velocity profile reads:

$$\begin{aligned} u^+_{SA}(y^+) &= c_1 \ln((y^+ + a_1)^2 + b_1^2) - c_2 \ln((y^+ + a_2)^2 + b_2^2) \\ &- c_3 \,\mathrm{ArcTan}[y^+ + a_1, b_1] - c_4 \,\mathrm{ArcTan}[y^+ + a_2, b_2)] + \overline{B}, \end{aligned} \tag{1}$$

where $\mathrm{ArcTan}[x, y]$ is the Mathematica function that gives the arc tangent of y/x, taking into account which quadrant the point (x, y) is in. We recall that the exponent "+" refers to wall units, i.e. $u^+ = u/u_\tau$ and $y^+ = yu_\tau/\nu_w$, where u_τ

denotes classically the friction velocity.
The constant parameter values are:

$\overline{B}$=5.0333908790505579 ,
a_1=8.148221580024245 , a_2=-6.9287093849022945
b_1=7.4600876082527945 , b_2=7.468145790401841
c_1=2.5496773539754747 , c_2=1.330165158853522 8
c_3=3.599459109332379 , c_4=3.6397531868684494.

This law is supplemented with the theoretical near wall expression of the pseudo-turbulent viscosity, *i.e.* $\tilde{\nu} = \nu\kappa y^+$. However, using directly relation (1) at the near-wall forcing points may lead in most cases to the implicit introduction of too steep velocity gradients, not supported by the grid when using a low-order numerical scheme. For this reason, we consider in this study a modification of the model, inspired by the velocity linearization process introduced by Capizzano [21] and later on by Tamaki *et al.* [22]. This method ensures an acceptable reconstruction of the wall-normal velocity derivative in the numerical solver. The tangential velocity component at the forcing point near the wall "F" $u_{t,F}$ at $y = y_F$ is therefore re-written as:

$$u^+_{t,F} = u^+_{SA}(y^+_{IP}) - \left(y^+_{IP} - y^+_F\right) \frac{\partial u^+_{SA}}{\partial y^+}\left(y^+_{IP}\right) \tag{2}$$

where the subscript "IP" denotes the near-wall interpolated point in the fluid that is used to evaluate the friction velocity u_τ thanks to a Newton iterative process. This relation therefore ensures a linear behavior of the velocity below the linearization distance $y = y_{IP}$, with a wall-normal velocity derivative consistent with the wall law at $y = y_{IP}$.
As detailed by Tamaki *et al.* [22], a near-wall modification of the SA model is required when using this velocity linearization process given by Equation (2), in order to ensure the conservation of the total shear stress. The near-wall modification of the SA f_{v1} damping function proposed in [22] is used to do so. For any point at a distance y from the wall, the turbulent viscosity is then evaluated as:

$$\nu_t = r_d f_{v1}\left(r_d \chi\right)\tilde{\nu} \quad , \quad \text{with } \chi = \frac{\tilde{\nu}}{\nu} \tag{3}$$

instead of the classical expression $\nu_t = f_{v1}\left(\chi\right)\tilde{\nu}$. Here, f_{v1} denotes the classical damping function of the standard Spalart-Allmaras turbulence model and the modification is only effective by introducing the distance scaling factor r_d, defined as:

$$r_d = \frac{y_{IP}}{y} \text{ if } y < y_{IP}, \tag{4}$$

$$r_d = 1 \text{ elsewhere.} \tag{5}$$

It is easy to show that in the near-wall region, when the pseudo-viscosity evolves as $\tilde{\nu}(y) = \kappa u_\tau y$, relation (3) simplifies as $\nu_t(y) = \nu_t(y_{IP})$ if $y < y_{IP}$. Therefore, this ensures a constant total shear stress when $y < y_{IP}$, *i.e.* when the velocity profile is forced to evolve linearly according to relation (2).
The actual process considered in our study (not detailed here for the sake of brevity) is inspired by this linearization technique, but it relies on a different choice of the linearization distance. This makes it possible to ensure dynamically a better control of the numerical error.

2. Laminar boundary layers

In this study, a specific transition triggering strategy was adopted in the experiments.For that purpose, zig-zag transition strips were added on the tread of the wheels, at an angle of 60° with respect to the stagnation point on the front of the wheels. This effect must be reproduced in the simulations. Although it is usual to adopt specific modifications of the SA turbulence model, it turns out to be not sufficient and the wall law must be modified as well in laminar flow regions. In laminar regions, the wall law is therefore reformulated uging a second order polynomial, *i.e.* : $u(y) = ay^2 + by + c$, where $c = 0$ to ensure the no-slip condition at the wall. The two remaining coefficients a and b are evaluated for each forcing point by using a second row of interpolated points located at $y_{IP,2} = 1.2y_{IP}$. This allows to derive the following linear system to obtain a and b:

$$y^2_{IP}a + y_{IP}b = u_{IP} \tag{6}$$

$$y^2_{IP,2}a + y_{IP,2}b = u_{IP,2} \tag{7}$$

It must be noted that this laminar wall law will also be used in specific flow regions where the Reynolds number is too low to develop turbulent boundary layers, *e.g.* on the leg of the landing gear. This point will be briefly discussed in Section IV.

C. Wire mesh screen model

The wire mesh screen model retained in this study is the same as the one previously developed in [7]. This model represents the wire mesh screen using a fictitious boundary, immersed in the computational domain. As it is done for the wall modeling, forcing points are introduced in the vicinity of the wire mesh, where the flow variables are modified to account for its presence. Two fringes of forcing points are introduced, on both sides of the screen. Each side is referred to as upstream ("up") or downstream ("down"), depending on the orientation of the local velocity vector with respect to the normal vector to the wire mesh surface. The model accounts for three main effects: a pressure drop across the wire mesh, flow deflection and turbulence generation at small scales.

These three effects are achieved by defining appropriate values for pressure, velocity and turbulent viscosity at the wire mesh location. The model was carefully calibrated using empirical relations from literature and dedicated Direct Numerical Simulations of isolated wire mesh samples [7]. The final expressions for the flow variables are recalled hereafter. For more details, the interested reader may refer to [7].

1) The pressure at the forcing points is given by:

$$p = p_w + s_w \frac{K}{4} \rho_{up} u_{i,up}^2, \tag{8}$$

where $p_w = \frac{1}{2}\left(p_{up} + p_{down}\right)$ and $s_w = 1$ upstream of the wire mesh or -1 downstream. The pressure drop coefficient K is given by[23]:

$$K \simeq \left(0.5 + 26 Re_d^{-1}\right) \frac{1-\beta^2}{\beta^2}, \tag{9}$$

In this expression, Re_d denotes the Reynolds number based on the wire diameter and the upstream velocity magnitude and β is the porosity coefficient of the wire mesh.

2) The velocity vector is decomposed between its normal (u_n) and tangential (u_t) components with respect to the surface. On the one hand, the normal component is kept unchanged through the wire mesh, *i.e.* :

$$u_n = u_{n,up} \tag{10}$$

On the other hand, a damping term is applied to the tangential component as:

$$u_t = \Delta_v \, u_{t,up}. \tag{11}$$

where the deflection coefficient is expressed as[24]:

$$\Delta_v = \frac{u_{t,down}}{u_{t,up}} \simeq \left[\left(\frac{K}{4}\right)^2 + 1\right]^{\frac{1}{2}} - \frac{K}{4} \tag{12}$$

3) Finally, turbulence generation at small scales is accounted for by altering the turbulent viscosity, to mimic the energy cascade to smaller scales. A mixing length model is retained and formulated using only the flow variables at the wire mesh location as:

$$\mu_t = \rho \, C_t \cdot d \cdot |u_w| \tag{13}$$

where $|u_w| = \sqrt{u_n^2 + u_t^2}$ and $C_t \simeq 0.065$ [7].

D. Numerical setup

A grid convergence study was first performed, with near-wall grid resolutions between 0.25 mm and 2 mm. A good trade-off between the quality of the results and the cost of the simulation was obtained with a near-wall grid resolution of 0.5 mm (*i.e.* $\Delta x_{min} = D/300$), for an overall moderate number of grid cells count of about 40 millions. This grid resolution will be adopted throughout this study.

Figure 7 (left) shows close-up views of the grids used respectively around the baseline configuration and the controlled

one (*i.e.* equipped with a fairing). The finest grid level (Δx=0.5 mm) is used near the solid walls, while a constant grid resolution of 1 mm is adopted in the wake region to ensure a proper resolution of the turbulent structures. The grid is then gradually coarsened using an Octree strategy, up to a distance of about 30 wheel diameters. Figure 7 (right) displays a view of the full computational domain, with the boundary conditions. It is worth noting that a slip boundary condition is used at the top of the domain, to mimic the presence of the "fuselage" flat plate in the experiments.
We recall that all the simulations presented in this study have been performed for the highest inflow velocity value considered in the wind tunnel tests, *i.e.* $U_\infty = 35$ m/s.
In all cases, the flow statistics are collected after a transient time of 120 ms. The sampling duration for the statistics is 100 ms. The time step used in the simulations is $\Delta t = 5 \times 10^{-6}$ s.

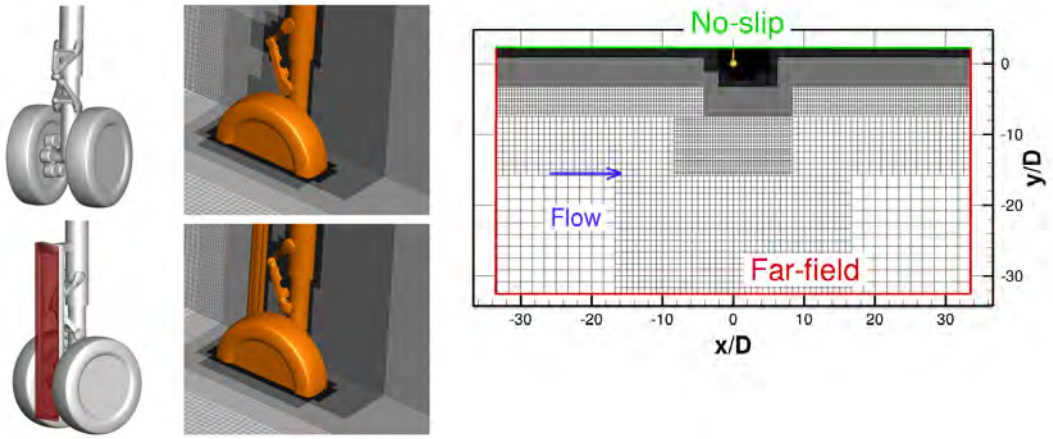

Fig. 7 Left: landing gear configurations and close-up view of the grids used. Top: baseline configuration. Bottom: controlled configuration with fairing and support. Right: Overall view of the computational domain, in the symmetry plane.

IV. Simulation of the baseline landing gear configuration

First we present in this section the assessment of the computational approach to the simulation of the baseline case, *i.e.* the two-wheel landing gear equipped with the brakes and the torque link.

A. Effect of the wall law

As mentioned earlier, several regions of the flow are laminar, *e.g.* the boundary layers developing on the front of the wheels, before the triggering device, or on the leg of the landing gear. Indeed, the leg is composed of a cylindrical strut, with a diameter of 35.5 mm. In the present flow conditions, the leg diameter-based Reynolds number is about 87,000. This may lead to a flow in the subcritical regime, where the boundary layers do not have yet undergone transition to turbulence. The same remark holds for the axle between the wheels and the brakes elements. In such a case, the application of a classical "turbulent" wall law everywhere is therefore questionable. For that reason, three possible strategies based on the turbulent wall law, laminar wall law, or a hybrid combination of these two laws have been tested (*i.e.* laminar wall law applied only on the leg, torque link, wheel axle and brake elements). It is worth noting that in all cases, the flow and the wall law are both set to laminar mode in the front part of the wheels tread.
Figure 8 presents instantaneous snapshots of the flow for the three aforementioned cases. It is clear that the switch from the turbulent SA wall law to the laminar one results in massive changes on the flow topology: the flow separation on the main leg and torque link occurs earlier when the laminar wall law is used, resulting in a different development of the wake. When the laminar wall law is also applied on the wheels side, a massive separation is observed in that

region, with the occurrence of a Kelvin-Helmholtz instability in the shear layer on the external sides of the wheels. These visualizations also highlight that the torque link appears as the main source of sound of the configuration.
A more detailed comparison of these three computations has been carried out, with a systematic assessment against the statistical experimental results. This point will not be detailed in the present paper for the sake of brevity, but on the basis of these results, the strategy based on the combination of the turbulent wall law and the laminar one will be adopted in the rest of the study.

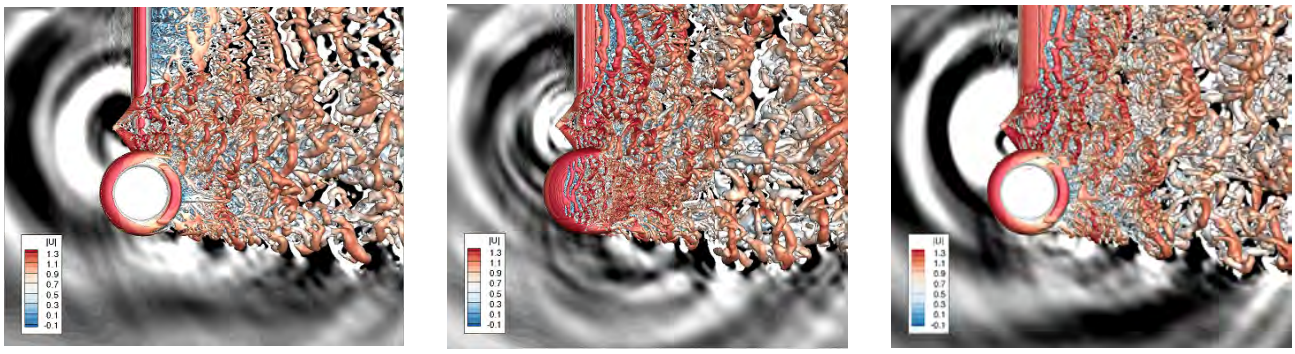

Fully turbulent SA wall law | Laminar wall law everywhere | Laminar wall law on LG leg, wheel axle, torque link and brakes

Fig. 8 Effect of the wall law. In all cases, the flow and wall law are forced to laminar mode on the tread of the wheels up to ±60° from the stagnation point. Iso-surfaces of the Q criterion are displayed, colored by the velocity magnitude. Black and white contours show the dilatation field in the symmetry plane.

B. Comparison with experimental results

This section presents the assessment of the ZDES simulation for the flow around the baseline configuration. We recall that for the following results, the combination of the SA wall law and the laminar one is adopted.
Figure 9 presents the mean flow velocity contours in the vertical plane located in the wake, at $x = 170$ mm. Overall, a very nice agreement with the PIV measurements is observed. The ability of the simulation to reproduce the main features of the flow is confirmed by looking at Figure 10 that presents the RMS velocity fluctuations in the same plane. Again, the agreement between the simulation and the PIV measurements is very good, for all the components of the resolved Reynolds stresses.
A similar agreement is observed in the horizontal plane at $y = 0$ mm, for both the mean and RMS quantitites (see Figure 11).
A more quantitative comparison is done in Figure 12, displaying some profiles of the mean velocity and RMS velocity fluctuations for several rakes along the spanwise direction, at $x = 170$ mm. The excellent agreement between the simulation and the measurements is confirmed, although some differences are observed in the wake region at the center of the wheels ($y = 0$ mm). At this specific location, the wake is a bit narrower in the simulation than in the experiment. This may be the consequence of the use of the fully turbulent SA wall law on the sides of the wheels, which probably delays a bit flow separation. However, the overall agreement between the simulation and the measurements is very good, even in the wake of the torque link where a highly complex flow is present.

V. Simulation of the controlled landing gear configurations

This section presents the numerical results obtained for the three controlled cases, *i.e.* with the solid fairing and the two wire meshes. Again, a comparison with the measurements is carried out. It is worth noting that the cases with the wire mesh fairings represent an important challenge for the modeling strategy presented in Section III.C.

A. Solid fairing

Figure 13 presents a comparison of the numerical results with the PIV measurements. For the sake of brevity, only a partial set of extraction planes is shown here. Although there is again a fair agreement between these results, some

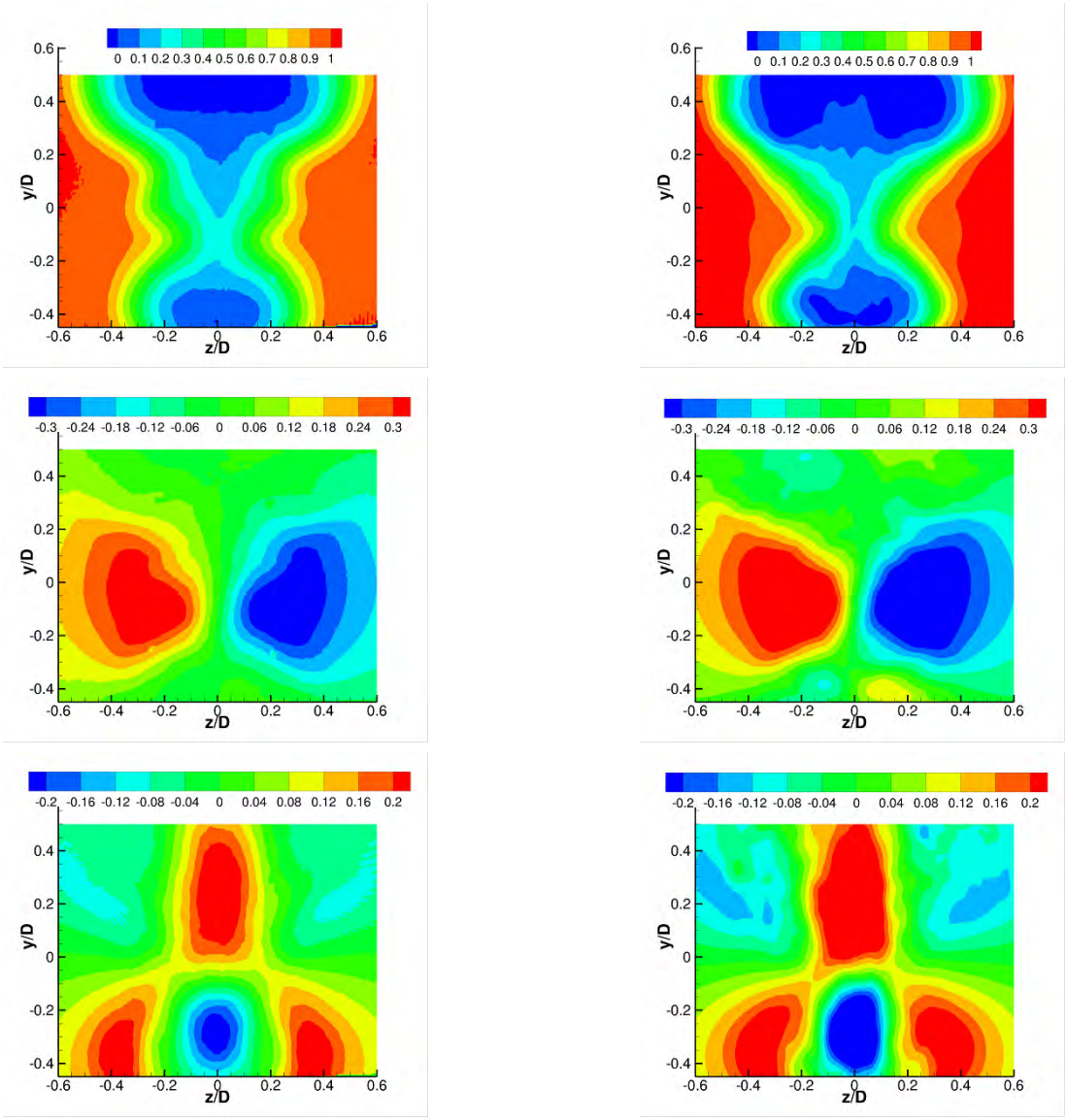

Fig. 9 Mean velocity for the baseline configuration at $x = 170mm$ ($x/D = 1.13$). Left: PIV; Right: ZDES Simulation. From top to bottom: u/U_∞, v/U_∞, w/U_∞.

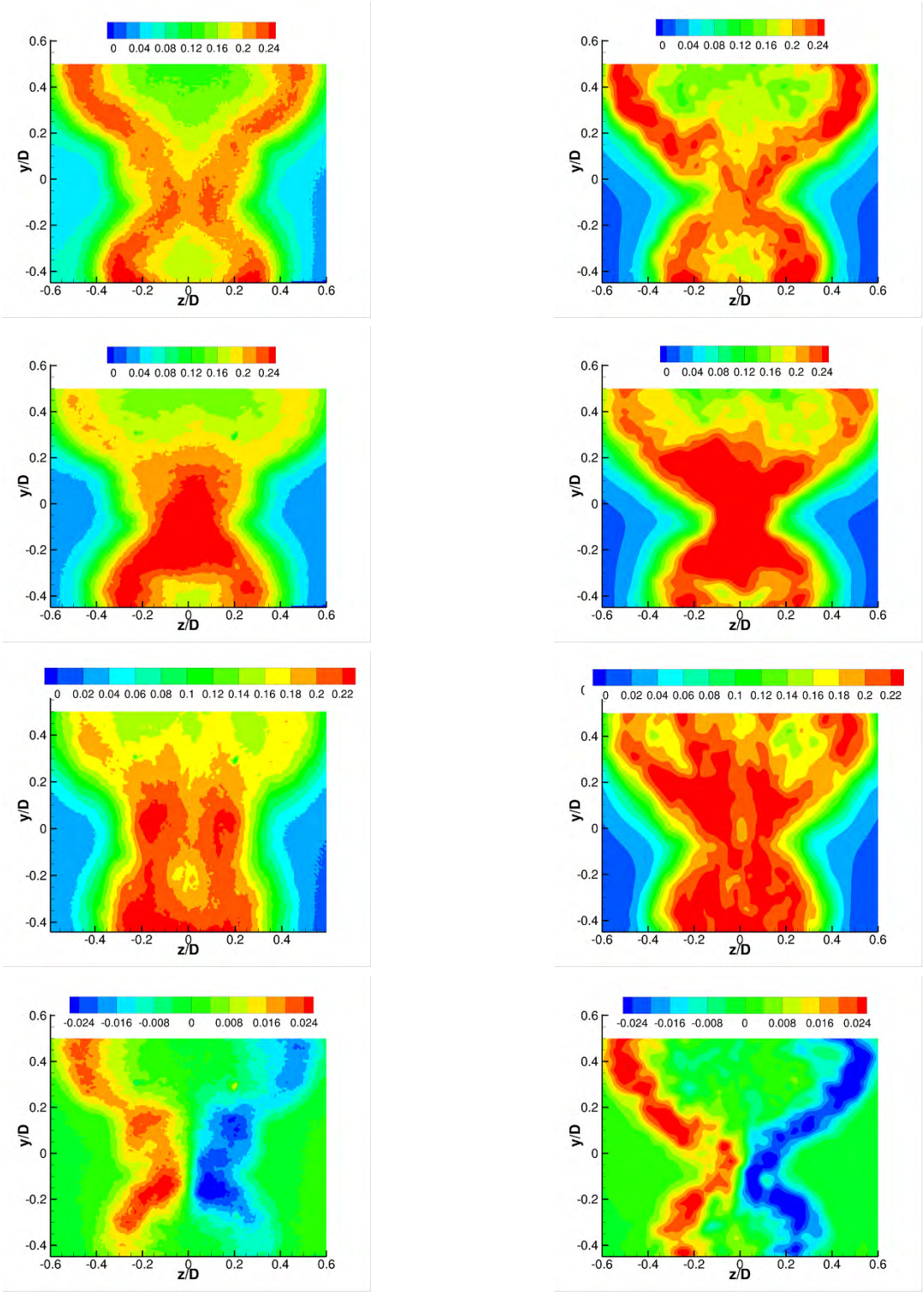

Fig. 10 Resolved RMS velocity fluctuations for the baseline configuration at $x = 170mm$ $(x/D = 1.13)$. Left: PIV; Right: ZDES Simulation. From top to bottom: u'/U_∞, v'/U_∞, w'/U_∞, $u'w'/U_\infty^2$.

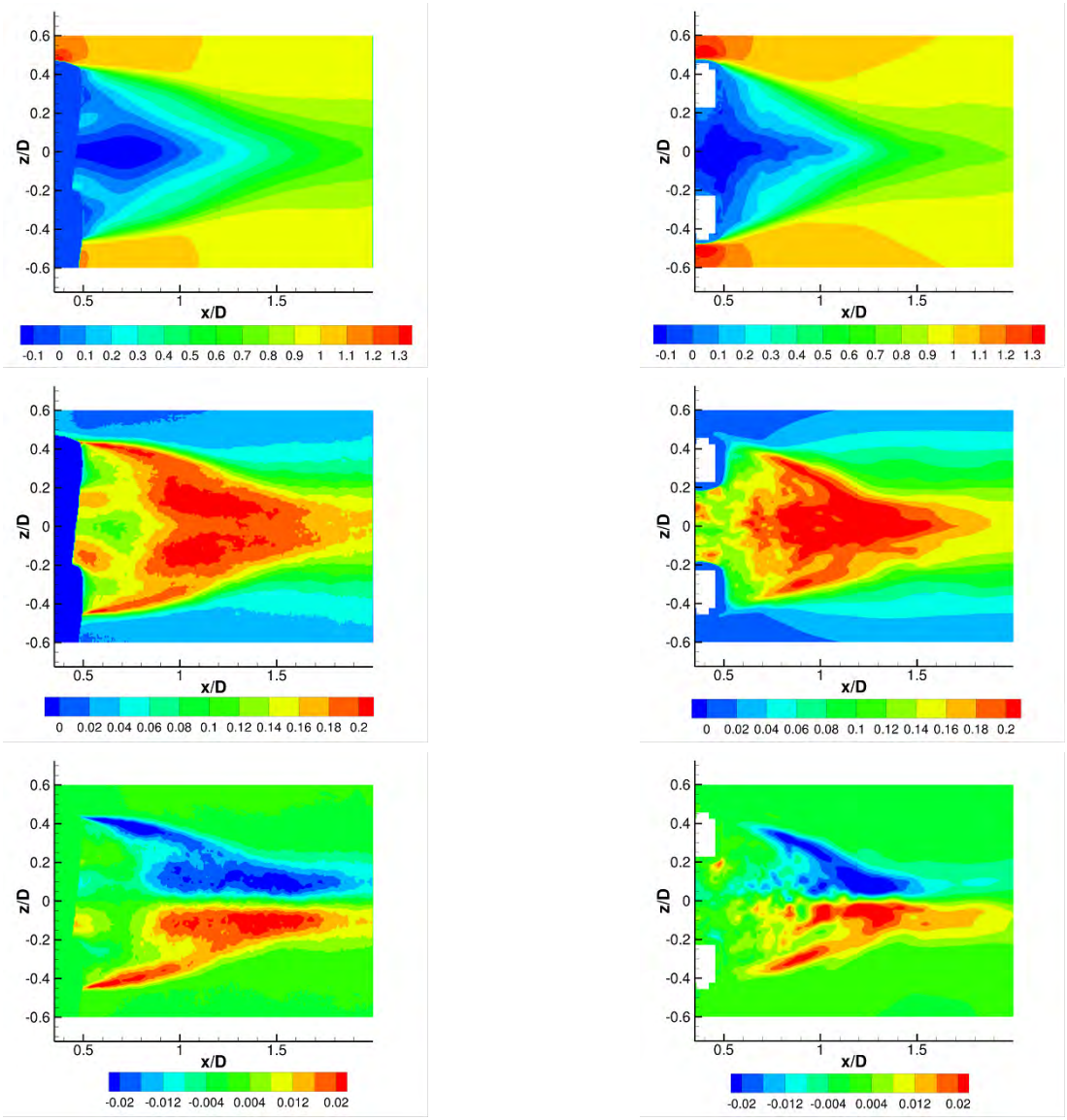

Fig. 11 Mean velocity and RMS velocity fluctuations for the baseline configuration at $y = 0mm$. Left: PIV; Right: ZDES Simulation. From top to bottom: u/U_∞, u'/U_∞, $u'w'/U_\infty^2$.

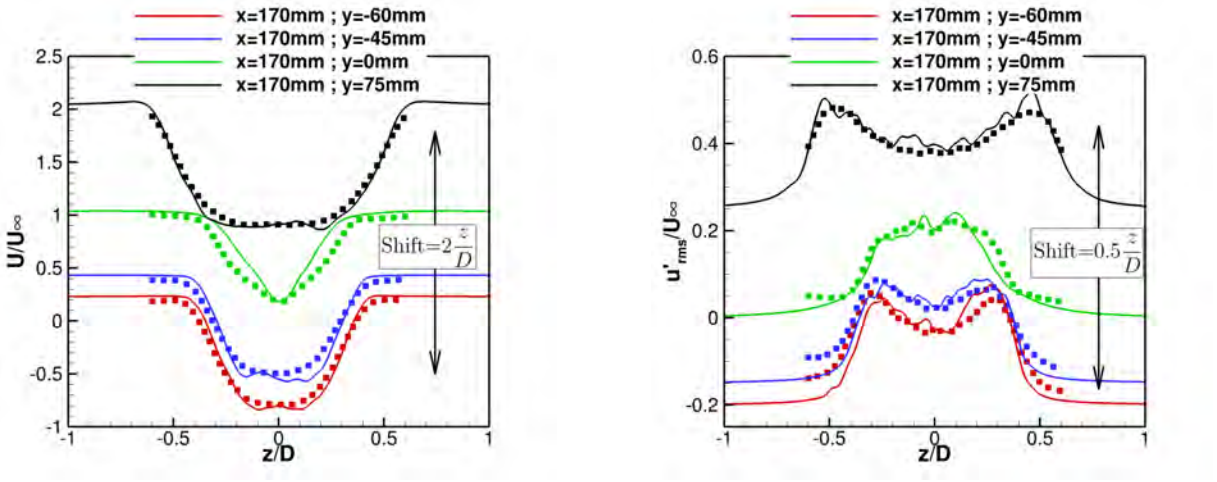

Fig. 12 Mean and RMS velocity profiles at $x = 170mm$ ($x/D = 1.13$) for the baseline configuration. Left: mean streamwise velocity u; Right: streamwise RMS velocity fluctuations u'. Symbols: experiment; solid lines: ZDES simulation.

differences remain in the wake at the center of the wheels. Indeed, Figure 13 suggests that a flow deceleration is present on the external sides of the wheels in the experiment, which is not present in the simulation. Again, we suspect that this could be an effect of the wall law used on the sides of the wheels. Indeed, the presence of the fairing is probably responsible for a strong adverse pressure gradient on the wheels sides, which is not accounted for by the wall law. This represents a challenging issue that will be considered in future studies, by modifying the wall law, or by refining the grid in these critical areas.

Figure 14 presents the mean and RMS velocity profiles extracted along the same rakes as it was done for the baseline case. As it could be anticipated from the velocity contours analysis, the agreement between the simulation and the measurements is fair, except at $y = 0$ mm, where the RMS velocity fluctuations are over-estimated. This may be the consequence of a different wake development in this area, probably due to the aforementioned different flow behaviors on the wheels sides.

B. Wire mesh fairings

In this section, the results obtained using the two wire mesh fairings are presented. First of all, the mean and RMS velocity components extracted on the previous rakes are displayed in Figure 15 and compared to the measurements for both wire meshes. Overall the agreement between the simulations and the PIV measurements is fair, although some discrepancies are still present at $y = 0$ mm. However, the mean velocity magnitude and velocity fluctuations are well predicted by the simulations, which indicates that the wire mesh numerical model is efficient to properly reproduce the partial blockage of the flow at the fairing location. This is confirmed by looking at Figures 16 and 17 presenting mean and RMS velocity contours in the horizontal plane located at $y = 120$ mm, *i.e.* in the wake of the torque link. The results are also compared to those obtained using the solid fairing. There, the agreement between the simulations and the PIV measurements is very good, for both the mean value and the resolved fluctuations. It is noticeable that the blockage effect of the fine wire mesh is significantly more important than the one from the coarse wire mesh. The fine wire mesh seems to act in a very similar way as the solid fairing, with a low permeability and an important velocity reduction. It is worth noting that the acoustic measurements (see Section VI.B) exhibit very similar noise reduction properties for the solid fairing and the fine wire mesh, over the whole range of measured frequencies. This is consistent with the very similar flow topologies observed in the simulations.

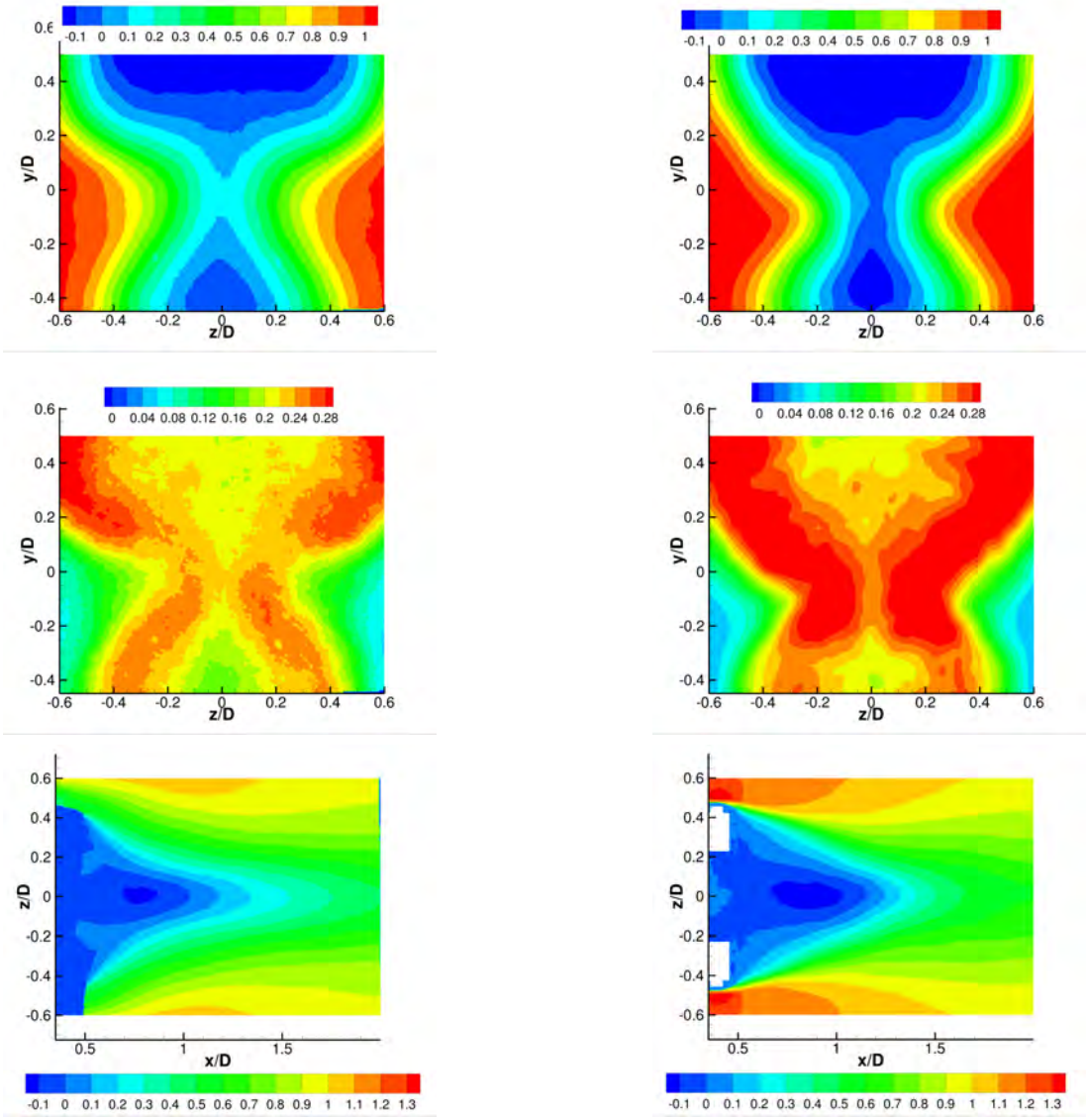

Fig. 13 Velocity statistics for the solid fairing configuration. Left: PIV; Right: Simulation. From top to bottom: u/U_∞ **at** $x = 170mm$ $(x/D = 1.13)$**,** u'/U_∞ **at** $x = 170mm$ $(x/D = 1.13)$ **and** u/U_∞ **at** $y = 0mm$**.**

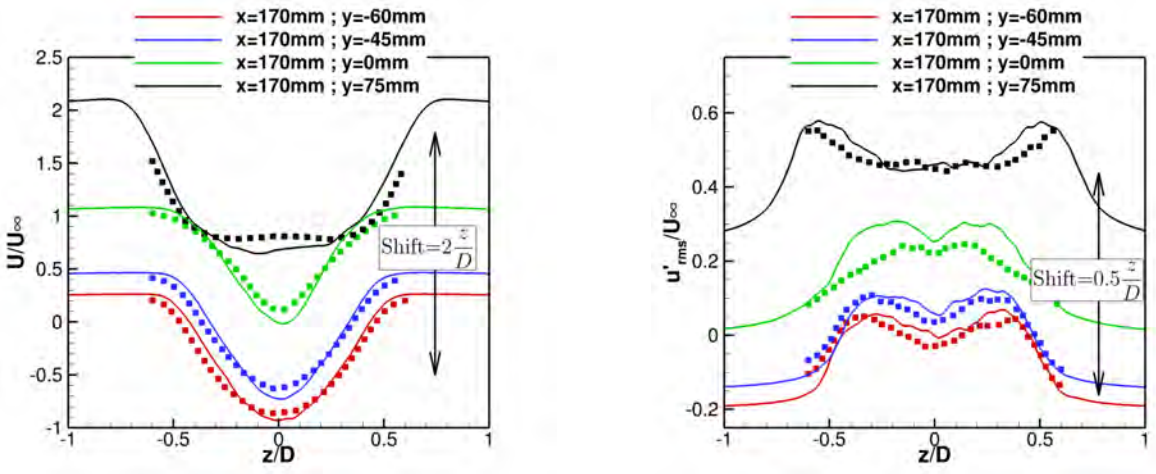

Fig. 14 Mean and RMS velocity profiles at $x = 170mm$ ($x/D = 1.13$) for the solid fairing configuration. Left: mean streamwise velocity u; Right: streamwise RMS velocity fluctuations u'. Symbols: experiment; solid lines: ZDES simulation.

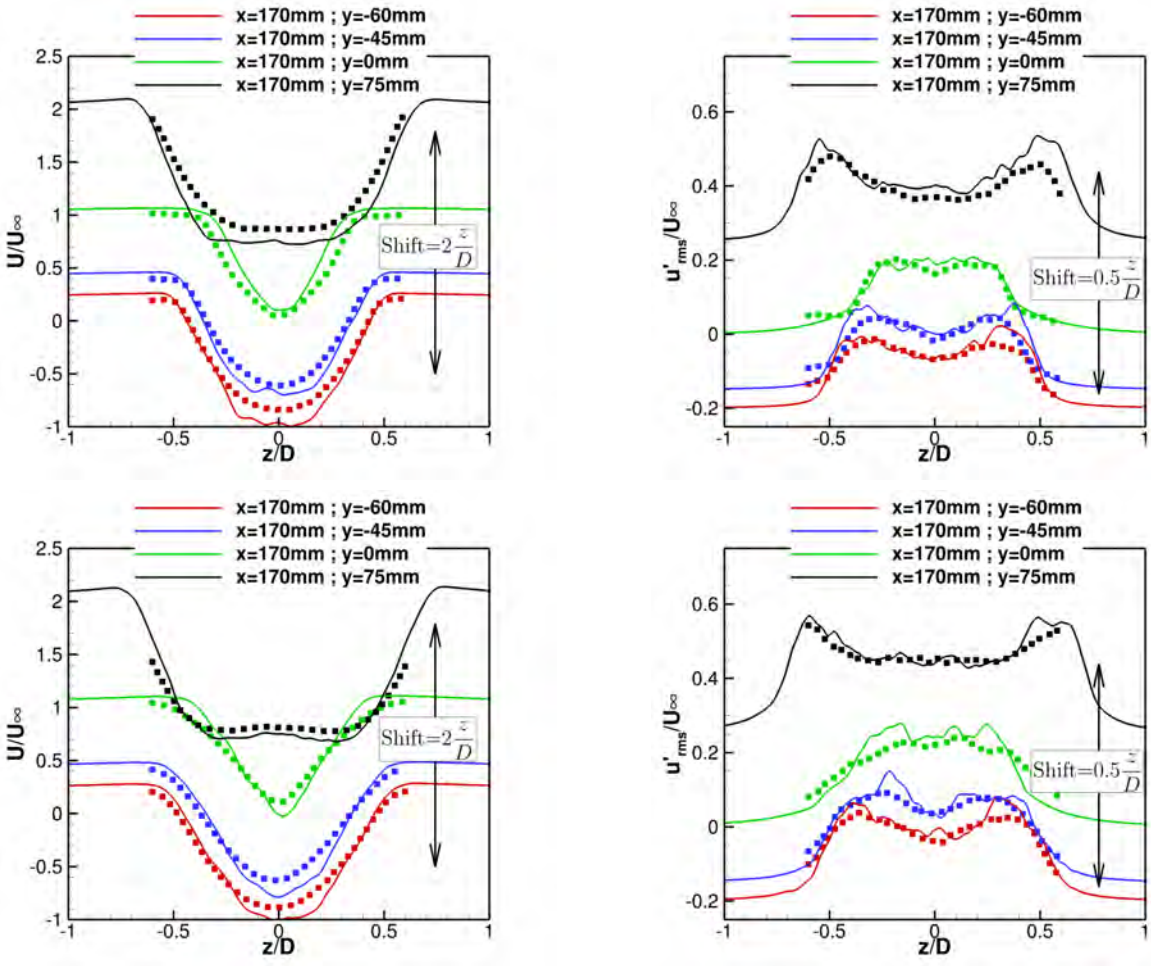

Fig. 15 Mean and RMS velocity profiles at $x = 170mm$ $(x/D = 1.13)$ for the wire mesh fairings configurations. Left: mean streamwise velocity u; Right: streamwise RMS velocity fluctuations u'. Top: coarse wire mesh; Bottom: Fine wire mesh. Symbols: experiment; solid lines: ZDES simulation.

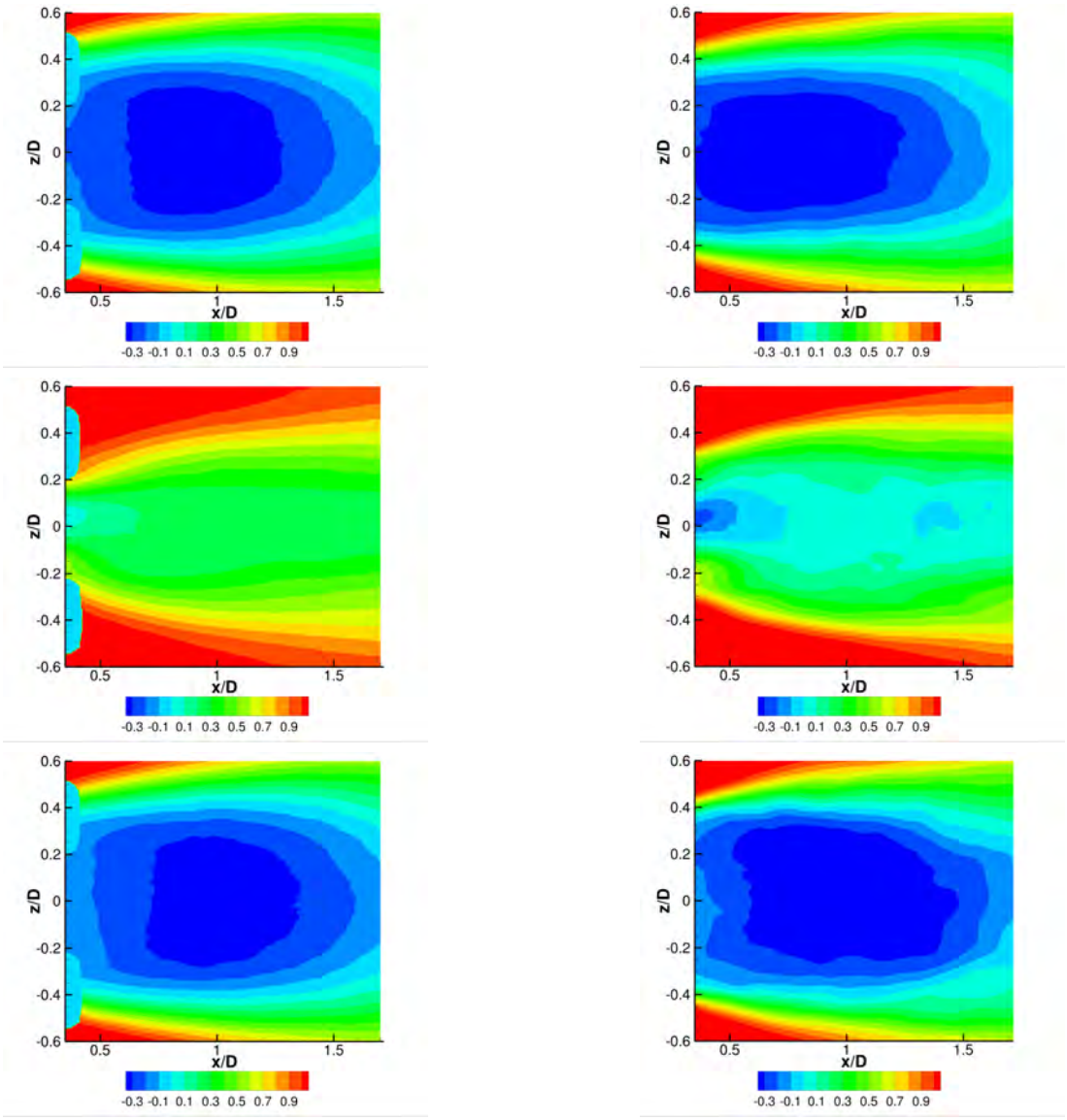

Fig. 16 Mean streamwise velocity u/U_∞ for the wire mesh fairings configurations at $y = 120mm$ $(y/D = 0.8)$. Left: PIV; Right: ZDES Simulation. Top: solid fairing; Middle: coarse wire mesh; Bottom: Fine wire mesh.

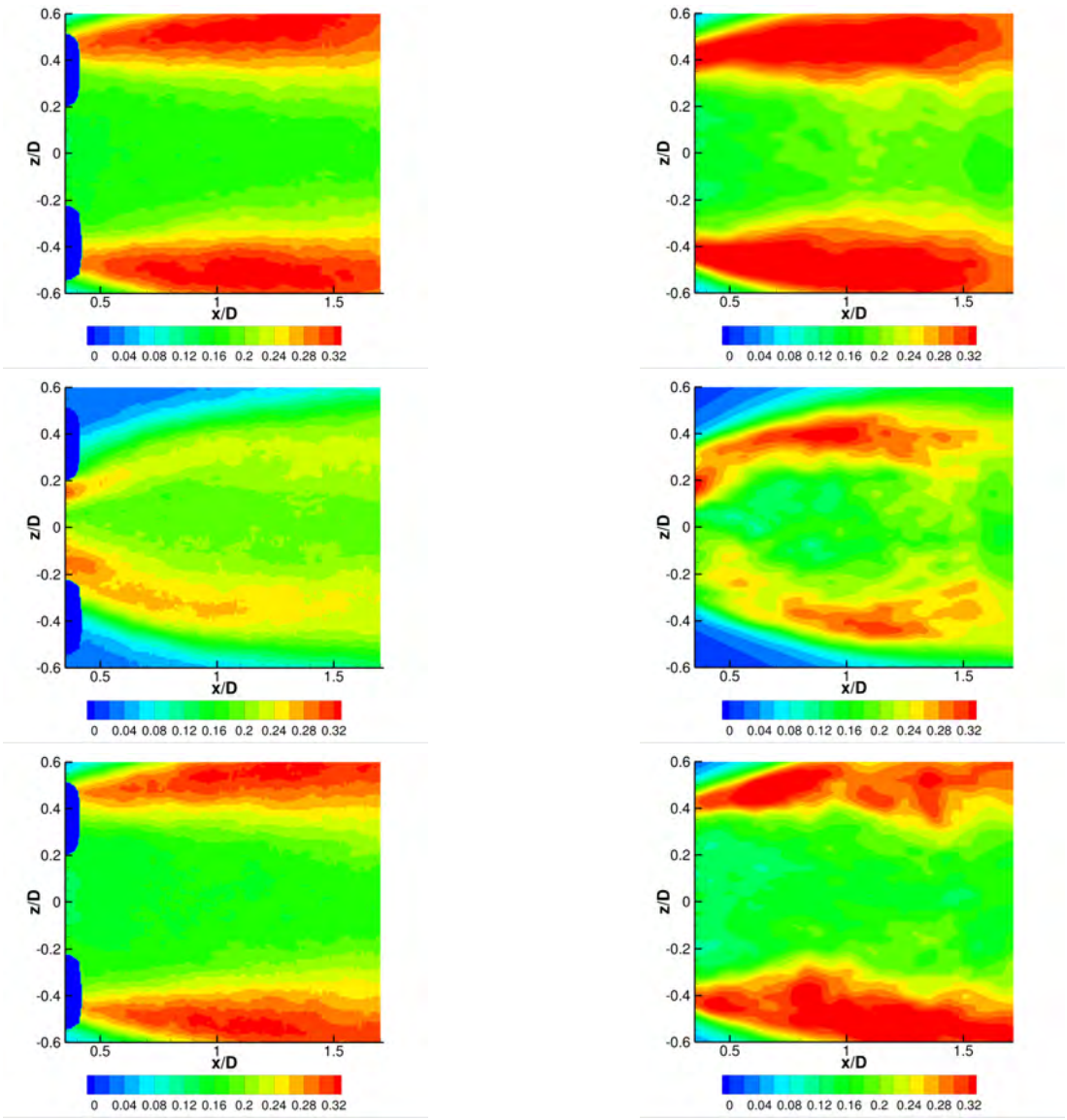

Fig. 17 RMS streamwise velocity fluctuations for the wire mesh fairings configurations at $y = 120mm$ $(y/D = 0.8)$. Left: PIV; Right: ZDES Simulation. Top: solid fairing; Middle: coarse wire mesh; Bottom: Fine wire mesh.

VI. Physical analysis of the fairing's effect and noise mitigation properties

The results presented in the previous sections clearly demonstrate that the chosen numerical approach is able to fairly reproduce the flow around the landing gear, with and without fairing. Both solid and wire mesh fairings could be considered, thanks to the numerical wire mesh model presented in Section III.C. In all cases, an overall good agreement between the measurements and the simulations has been obtained. This numerical approach therefore appears as a valuable tool to analyze the flow modifications implied by these devices and possibly optimize their characteristics. The present section is devoted to the physical analysis of the flow for the four different configurations considered in this study: Subsection VI.A provides an insight into the noise sources identifications and flow modifications provided by the fairings, while the resulting far-field acoustics and noise mitigation aspects will be presented in Subsection VI.B.

A. Noise sources identifications

The simulations carried out in this study offer the ability to get a detailed insight into the flow features that might be responsible for noise sources mitigation effects, at spatial locations that are not easily accessible during wind tunnel measurements (e.g. between the wheels or downstream of the fairing). To illustrate this point, Figure 18 presents the distribution of the pressure fluctuations on the landing gear surface, while Figure 19 presents some snapshots of the velocity magnitude in the plane $y/D = 0.165$, located very close to the internal face of the right wheel.

For the baseline geometry, it appears that two main regions are responsible for noise generation. The first one is located on the main strut of the landing gear, where the wake of the torque link impinges on the surface. This spot is divided into two sub-regions that correspond respectively to the impingement of high velocity wakes originating from the two large holes present in the torque-link (see Figure 1). The second main area responsible for noise generation is located in the downstream part of the internal sides of the wheels, where the complex separated flow generated by the main strut, wheel axle and the brakes impinges on the wheels. Again, two sub-regions are observed and are linked to strongly accelerated vortical flow patterns on each side of the brakes, that impinge on the wheel's surface.

These two main noise sources disappear completely when the solid fairing is applied, because the high-velocity flow around the torque link, main strut and brakes is almost completely suppressed, due to the shielding effect of the fairing. However, a secondary noise source is observed at the upper junction between its support and the main strut. Looking at Figure 19, it appears that this source is due to a mixing layer generated at the upper part of the fairing, where shear layer instabilities impinge on the strut. The contribution of this secondary noise source to the overall radiated noise will be discussed later on. The coarse wire mesh provides, as it could be expected, a partial shielding effect. As a consequence, the primary noise sources observed on the baseline configuration are still observed, but with a significantly lower intensity, due to flow deceleration. The secondary noise source at the top of the support is however still present. Finally, as it was already suggested by the flow comparisons performed in Section V, the fine wire mesh leads to a distribution very close to the one of the solid fairing *i.e.* its shielding effect is very high.

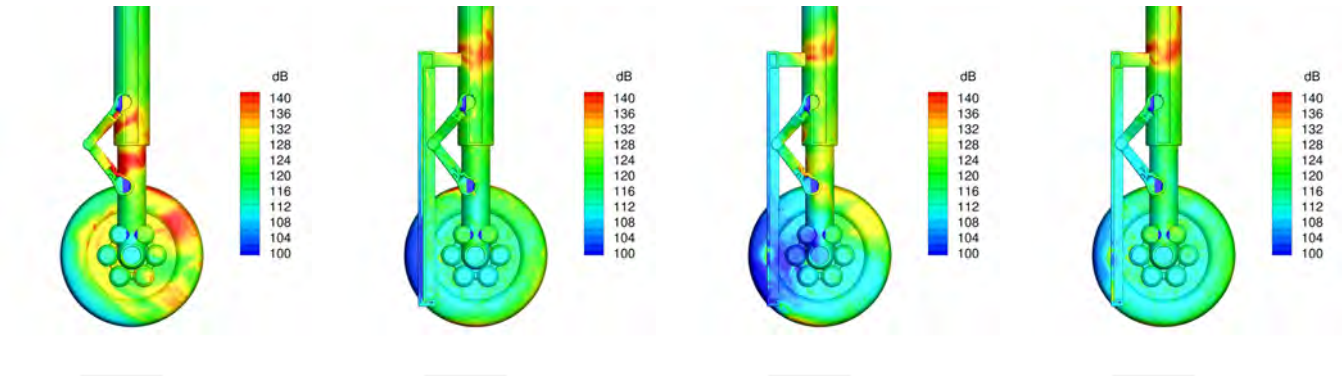

Fig. 18 Resolved RMS wall pressure fluctuations, in dB ($p_{ref} = 2 \times 10^{-5}$ Pa). Left wheel is removed for clarity.

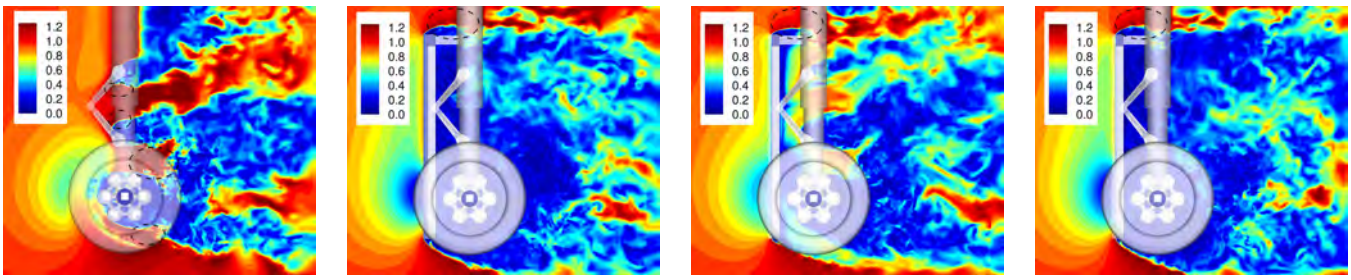

Fig. 19 Instantaneous velocity magnitude at $z/D = 0.165$.

B. Far-field Acoustics

This section presents the far-field acoustic results obtained from our simulations. For that purpose, the ONERA in-house code KIM [25] has been used to compute the acoustic far-field at 128 observer points, corresponding to each microphone from the experimental facility. We consider the solid formulation of the Ffowcs Williams-Hawkings (FW-H) equation [26], which requires the unsteady sampling of the pressure at the wall. In the context of Immersed boundary methods, this sampling can become quite tricky, since the wall is not explicitly present in the simulation. Common strategies introduce spatial interpolation of the pressure field to get its value at the wall. However this can introduce numerical errors that may compromise the accuracy of the acoustic post-processing. Instead, in this study, the stepwise surface reconstruction strategy developed by Manueco *et al.* [27, 28] has been adopted for the wall pressure unsteady data extraction. Indeed, this method appears of great interest in the present case, as it does not introduce any interpolation of the flow variables. This ensures a very accurate sampling of the wall pressure fluctuations, with no additional numerical filtering. A total sampling time of 80 ms is considered for the FW-H calculation.

Figure 20 (left) presents the acoustic spectrum obtained at the central microphone of the acoustic antenna in the the flyover position, for the baseline configuration. It is worth noting that both the numerical and experimental pressure signals have been post-processed using the exact same method and parameters, although 20 s of signal is available in the experiments. From this Figure, it appears that the agreement between the simulation and the measurements is not satisfactory. In the frequency range of interest, the overall level is over-estimated by about 5 dB in the simulation, which is not acceptable. A similar discrepancy is also observed for the three simulations with the fairings.

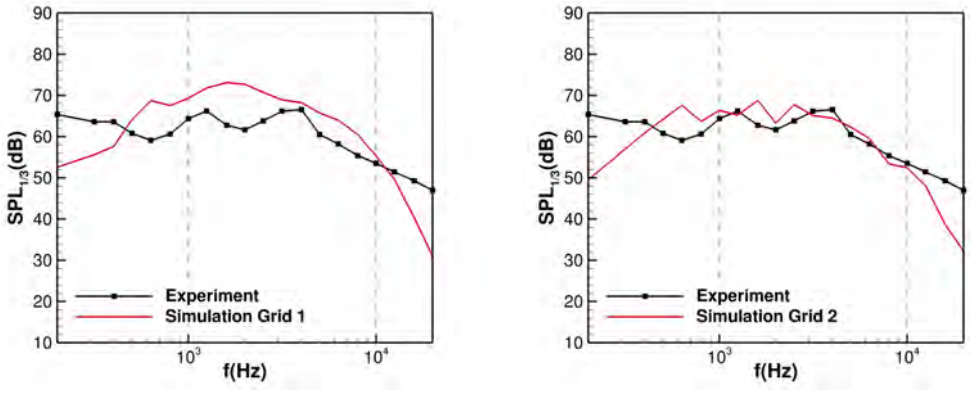

Fig. 20 Sound pressure level at the central flyover microphone for the baseline configuration (third-octave band dB, $p_{ref} = 2 \times 10^{-5}$Pa). See Figure 21 for grids 1 and 2 differences.

Considering the fair agreement obtained between the simulations and the experiments for the aerodynamic quantities, the most plausible explanation for these discrepancy is the occurrence of spurious noise at the interfaces between adjacent computational blocks with different spatial resolution. This is very critical in the wake region, where large

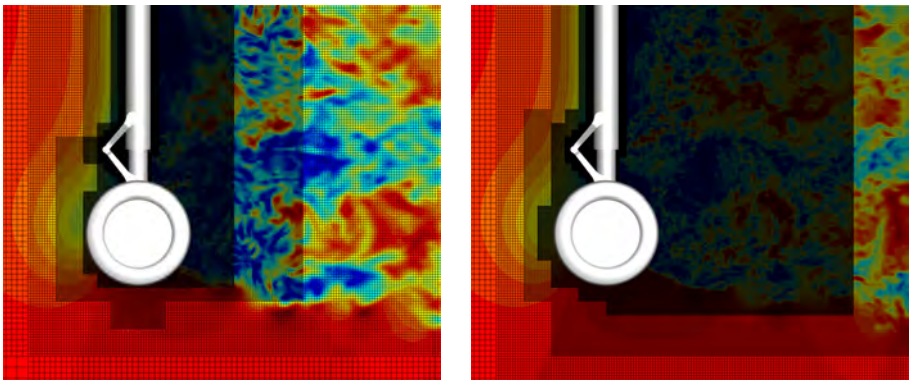

Fig. 21 Left: original grid (grid 1); Right: refined grid (grid 2).

packets of vortices cross such interfaces. To confirm this, an additional simulation has been carried out, for the baseline case only, on a new grid which is much more refined downstream of the landing gear. This should allow a better development of the turbulent wake, with a sufficient spatial extent to develop properly and dissipate the energy from the large structures before crossing the interface. This new grid (referred to as grid 2), compared to the original one in Figure 21, is composed of about 93 millions of cells.

Although the flow statistics have been barely affected by this grid refinement, a significant change is observed on the far-field noise prediction. Indeed, Figure 20 (right) exhibits a fair agreement between the simulation on the refined grid and the measurements for the radiated field. Unfortunately, the simulations on the refined grid could not be carried out at the present time for the landing gear equipped with the fairing. This will be done in future works. In the following, we will compare the results obtained on the original grid (grid 1) from a qualitative point of view, although a quantitative agreement with the experiments could not be obtained.

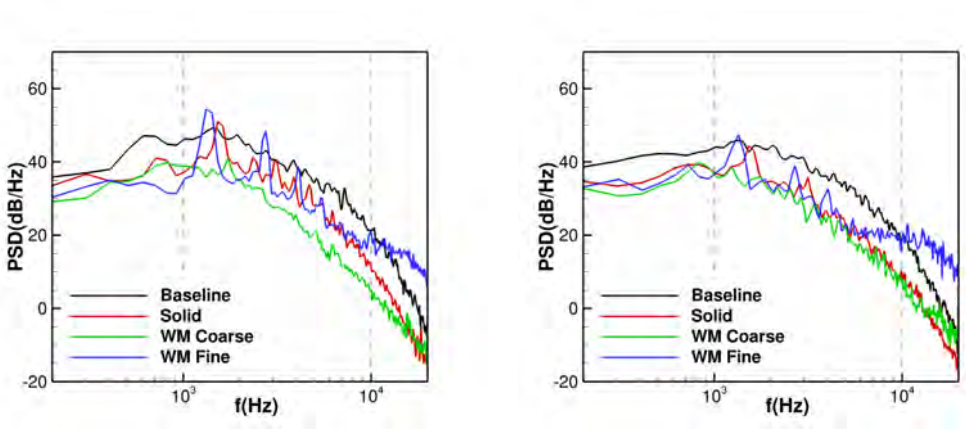

Fig. 22 Narrow-band acoustic power spectral density computed at the central acoustic antenna microphones (in dB, $p_{ref} = 2 \times 10^{-5}$Pa). Left: flyover position; right: sideline position.

Figure 22 presents the narrow-band spectra obtained for each configuration at the central microphones of the acoustic antenna, in the flyover and sideline positions. First of all, all the configurations equipped with a fairing lead to a substantial overall level reduction of the radiated noise. The fine wire mesh and the solid fairings lead to similar noise levels, except in the highest frequencies, where the fine wire mesh introduces additional noise. The exact reason for that has not yet been identified and will require additional investigations on a refined grid. The configuration with the coarse wire mesh fairing leads to the most important noise mitigation effect, which is surprising considering the near field observations. Again, this will require more investigations, using an adapted grid. It is striking that for the solid and fine

wire mesh fairings, strong tonal peaks with harmonics are present in the spectra. As already discussed, this is actually linked to the additional noise source present at the top of the fairing. Looking at Figure 23, we observe a large separated area at this extremity of the fairing, with the occurrence of a mixing layer. Large coherent K-H strutures are observed here, whatever the fairing. From these views, it is possible to get a rough estimate of the main frequency at which these vortices impinge on the main leg of the landing gear. Considering the distance l_v between two successive vortices and their approximate mean convection speed u_v, the obtained frequencies $f_v = u_v/l_v$ are respectively 1570 Hz, 1780 Hz and 1600 Hz for the solid, coarse wire mesh and fine wire mesh fairings. These estimates are in fair agreement with the observed main tonal peak frequencies in Figure 22. However, the wind tunnel measurements did not exhibit such peaks in the acoustic spectra. A detailed look on the grid close to the top of the fairings reveals that the initial thickness of the shear layers is not sufficiently discretized (see Figure 23). More seriously, the shear layer undergoes a jump in grid resolution. All this is certainly responsible for a delay in the development of the shear layer and its turbulent breakdown, so that the observed vortices are way too large and bi-dimensional. A finer single-resolution grid would certainly be necessary in this flow area, to allow a quicker transition to turbulence, with a broadband spectral signature. This point will also be addressed in future studies.

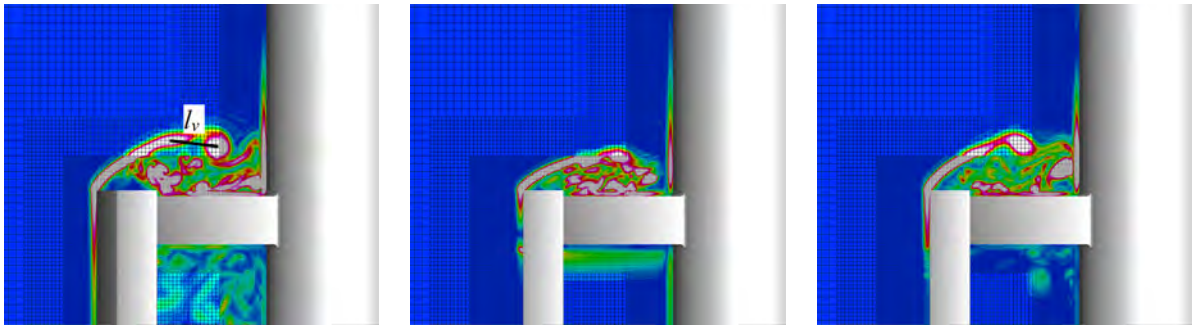

Fig. 23 Instantaneous spanwise vorticity in the central plane, at the top of the fairing.

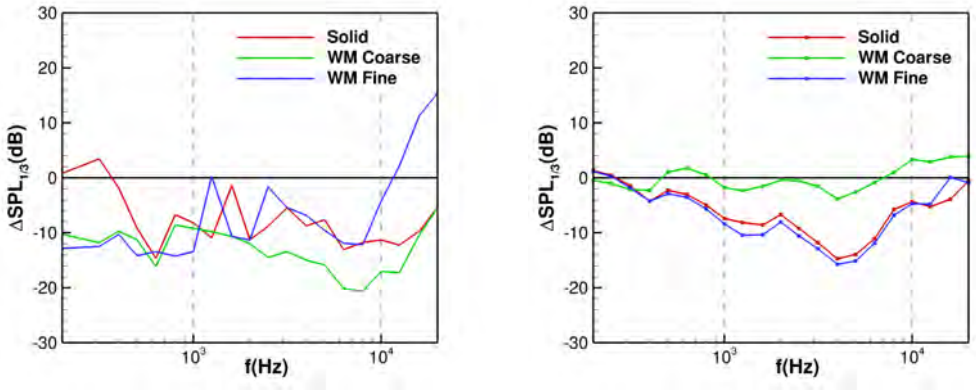

Fig. 24 Sound pressure level difference with respect to the baseline configuration (third-octave band dB, $p_{ref} = 2 \times 10^{-5}$Pa). Left: simulation; Right: Experiment.

Finally, Figure 24 presents the sound pressure level difference with respect to the baseline configuration, for the simulations (left) and the experiments (right). As already mentioned, the noise mitigation provided by the coarse wire mesh is very important in the simulations, which is not in agreement with the near field analysis. This will be further investigated in the future. The solid and fine wire mesh fairings provide similar noise mitigation over the frequency range of interest, by about 10 dB. Notice that the signature of the tonal peaks is still present at several frequencies and

should be discarded from the analysis. Overall, the noise reduction effect of these two fairing is comparable to the one observed in the experiments, although no quantitative agreement could be obtained for the far-field spectra using grid 1.

VII. Conclusions and future works

In this paper, we presented some of the results obtained during a joint experimental and numerical program on landing gear noise, which is part of the European project INVENTOR. We considered a simplified landing gear configuration, equipped with representative elements of a real aircraft (brakes and torque link), which are responsible for significant noise generation. Several cases have been investigated, including the baseline one and several configurations equipped with a fairing, made of solid or porous materials, such as the wire mesh fairings considered here.

In this study, a focus was made on the numerical simulations of these configurations, using a combination of the ZDES 2020 modeling approach [17] and an immersed boundary method carried out on octree Cartesian grids with wall models. For the wire mesh fairings, a specific model [7] has been used, in order to avoid a prohibitive direct resolution of all the wire mesh patterns.

The results from these simulations have been thoroughly compared to the PIV measurements. Overall, a nice agreement of the flowfield characteristics is obtained between the simulations and the experiments, whatever the configuration. This demonstrate the ability of the proposed modeling approach to properly simulate the flow around a landing gear configuration equipped with solid or wire mesh fairings.

Then, a thorough analysis of the flow patterns responsible for noise generation has been carried out. It was confirmed that high-speed separated flow regions through the torque link and around the brakes generate significant noise sources when impinging on the landing gear surface. The flow and noise sources modifications implied by the fairings have also been evidenced and basically reduce these noise sources by suppressing these high-speed flow regions. However, several issues have been pointed out regarding the far field noise prediction capabilities of our simulations, as the predicted noise levels overestimate the measured ones by about 5 dB. Therefore, the noise mitigation observations have to be taken with caution, although it was shown that the simulations predict comparable noise mitigation levels for the solid and fine wire mesh fairings (by 5 to 10 dB) with respect to the measurements. However, for the coarse wire mesh the predicted noise mitigation is too important and not consistent with the near field flow analysis, so that additional investigations are mandatory for this case. Nevertheless, it was shown that grid refinement in the wake of the landing gear greatly improves the noise prediction quality, during an additional simulation of the baseline configuration. It then appears necessary to re-conduct the simulations of the configurations equipped with fairings, using this refined grid. This could unfortunately not be achieved for the conference, but will be done in future works.

We will also consider the extension or adaptation of the present wire mesh model to other types of fairings, such as perforated plates or porous media (e.g. diamond-lattice meta-materials), as some of them also exhibited appreciable noise mitigation during the wind tunnel campaign. Indeed a large data base is available from the experimental works carried out in INVENTOR and will be used as reference. After a proper validation, this numerical approach will then represent a valuable tool to design and optimize dedicated fairings for a wide range of applied configurations.

Acknowledgments

This study received funding from the European Union's Horizon 2020 research and innovation programme within the project INVENTOR (INnoVative dEsign of iNstalled airframe componenTs for aircraft nOise Reduction) listed under the grant agreement ID: 860538.

The authors address special thanks to the other teams from the INVENTOR consortium involved in the noise mitigation with flow-trough fairings activity, who contributed to the fairings definition/manufacturing *i.e.* DLR, Dassault Aviation and VKI.

References

[1] Dobrzynski, W., Chow, L., Smith, M., Boillot, A., Dereure, O., and Molin, N., "Experimental assessment of low noise landing gear component design, 15th AIAA," *CEAS Aeroacoustics Conference*, 2009, pp. 11–13.

[2] Boorsma, K., Zhang, X., Molin, N., and Chow, L., "Bluff body noise control using perforated fairings," *AIAA Journal*, Vol. 47, No. 1, 2009, pp. 33–43. https://doi.org/http://dx.doi.org/10.2514/1.32766.

[3] Murayama, M., Yokokawa, Y., Yamamoto, K., and Hirai, T., "Computational study of low-noise fairings around tire-

axle region of a two-wheel main landing gear," *Computers & Fluids*, Vol. 85, 2013, pp. 114–124. https://doi.org/https://doi.org/10.1016/j.compfluid.2012.11.001.

[4] Khorrami, M. R., Lockard, D. P., Humphreys, W. M., and Ravetta, P. A., "Flight-Test Evaluation of Airframe Noise Mitigation Technologies," *2018 AIAA/CEAS Aeroacoustics Conference*, 2018, p. 2972. https://doi.org/https://doi.org/10.2514/6.2018-2972.

[5] Oerlemans, S., Sandu, C., Molin, N., and Piet, J., "Reduction of Landing Gear Noise Using Meshes,landing gear noise using meshes," AIAA Paper 2010-3972, 2010. https://doi.org/https://doi.org/10.2514/6.2010-3972.

[6] Okolo, P. N., Zhao, K., Kennedy, J., and Bennett, G. J., "Numerical Modeling of Wire Screens for Flow and Noise Control," *23rd AIAA/CEAS Aeroacoustics Conference*, 2017, p. 3700. https://doi.org/https://doi.org/10.2514/6.2017-3700.

[7] Terracol, M., and Manoha, E., "Numerical Wire Mesh Model for the Simulation of Noise-Reduction Devices," *AIAA Journal*, Vol. 59, No. 3, 2021, pp. 987–1007. https://doi.org/10.2514/1.j059548.

[8] Zhu, W., Xiao, Z., and Fu, S., "Numerical modeling screen for flow and noise control around tandem cylinders," *AIAA Journal*, Vol. 58, No. 6, 2020, pp. 2504–2516. https://doi.org/10.2514/1.J058636.

[9] Teruna, C., Avallone, F., Ragni, D., Rubio-Carpio, A., and Casalino, D., "Numerical analysis of a 3-D printed porous trailing edge for broadband noise reduction," *Journal of Fluid Mechanics*, Vol. 926, 2021. https://doi.org/http://dx.doi.org/10.1017/jfm.2021.704.

[10] Ferris, R., Appelbaum, J., and Khorrami, M. R., "Simulations of a full-scale aircraft with installed airframe noise reduction technologies," *2018 AIAA/CEAS Aeroacoustics Conference*, 2018, p. 2974. https://doi.org/https://doi.org/10.2514/6.2018-2974.

[11] Manoha, E., Bulté, J., and Caruelle, B., "LAGOON: an experimental database for the validation of CFD/CAA methods for landing gear noise prediction," *14th AIAA/CEAS aeroacoustics conference (29th AIAA aeroacoustics conference)*, 2008, p. 2816. https://doi.org/10.2514/6.2008-2816.

[12] Manoha, E., and Caruelle, B., "Summary of the LAGOON solutions from the Benchmark problems for Airframe Noise Computations-III Workshop," *21st AIAA/CEAS aeroacoustics conference*, 2015, p. 2846.

[13] Casalino, D., Ribeiro, A. F. P., Fares, E., and Nölting, S., "Lattice–Boltzmann Aeroacoustic Analysis of the LAGOON Landing-Gear Configuration," *AIAA Journal*, Vol. 52, No. 6, 2014, pp. 1232–1248. https://doi.org/10.2514/1.j052365, URL https://doi.org/10.2514/1.j052365.

[14] Merino-Martínez, R., Carpio, A. R., Pereira, L. T. L., van Herk, S., Avallone, F., Ragni, D., and Kotsonis, M., "Aeroacoustic design and characterization of the 3D-printed, open-jet, anechoic wind tunnel of Delft University of Technology," *Applied Acoustics*, Vol. 170, 2020, p. 107504. https://doi.org/10.1016/j.apacoust.2020.107504.

[15] Bennett, G. J., Lai, J., O'Brien, G., Ragni, D., Avallone, F., and Pott-Pollenske, M., "Flow Control and Passive Low Noise Technologies for Landing Gear Noise Reduction," *28th AIAA/CEAS Aeroacoustics 2022 Conference*, 2022, p. 2848. https://doi.org/10.2514/6.2022-2848.

[16] Mary, I., and Sagaut, P., "Large Eddy Simulation of Flow around an airfoil Near Stall," *AIAA journal*, Vol. 40, No. 6, 2002, pp. 1139–1145. https://doi.org/https://doi.org/10.2514/2.1763.

[17] Deck, S., and Renard, N., "Towards an enhanced protection of attached boundary layers in hybrid RANS/LES methods," *Journal of Computational Physics*, Vol. 400, 2020, p. 108970. https://doi.org/https://doi.org/10.1016/j.jcp.2019.108970.

[18] Spalart, P., and Allmaras, S., "A one-equation turbulence model for aerodynamic flows," *30th Aerospace Sciences Meeting and Exhibit*, American Institute of Aeronautics and Astronautics, 1992. https://doi.org/10.2514/6.1992-439.

[19] Benoit C., Péron S., and Landier S., "Cassiopee: a CFD pre- and post-processing tool," *Aerospace Science and Technology*, Vol. 45, 2015, pp. 272–243. https://doi.org/https://doi.org/10.1016/j.ast.2015.05.023.

[20] Allmaras, S. R., Johnson, F. T., and Spalart, P. R., "Modifications and clarifications for the implementation of the Spalart-Allmaras turbulence model," *Seventh international conference on computational fluid dynamics (ICCFD7)*, Big Island, HI, 2012, pp. 1–11.

[21] Capizzano, F., "Turbulent wall model for immersed boundary methods," *AIAA journal*, Vol. 49, No. 11, 2011, pp. 2367–2381.

[22] Tamaki, Y., Harada, M., and Imamura, T., "Near-Wall Modification of Spalart–Allmaras Turbulence Model for Immersed Boundary Method," *AIAA Journal*, Vol. 55, No. 9, 2017, pp. 3027–3039. https://doi.org/10.2514/1.j055824.

[23] Kurian, T., and Fransson, J. H., "Grid-generated turbulence revisited," *Fluid dynamics research*, Vol. 41, No. 2, 2009, p. 021403. https://doi.org/http://dx.doi.org/10.1088/0169-5983/41/2/021403.

[24] Gibbings, J., "The pyramid gauze diffuser," *Ingenieur-Archiv*, Vol. 42, No. 4, 1973, pp. 225–233. https://doi.org/https://doi.org/10.1007/BF00533610.

[25] Prieur, J., and Rahier, G., "Aeroacoustic integral methods, formulation and efficient numerical implementation," *Aerospace Science and Technology*, Vol. 5, No. 7, 2001, pp. 457–468. https://doi.org/10.1016/s1270-9638(01)01123-3.

[26] Ffowcs Williams, J., and Hawkings, D., "Sound generation by turbulence and surfaces in arbitrary motion," *Phil. Trans. Royal Soc.*, Vol. A 264, 1969, pp. 321–342.

[27] Manueco, L., Weiss, P.-E., and Deck, S., "On the estimation of unsteady aerodynamic forces and wall spectral content with immersed boundary conditions," *Computers & Fluids*, Vol. 201, 2020, p. 104471. https://doi.org/10.1016/j.compfluid.2020.104471.

[28] Manueco, L., Weiss, P.-É., and Deck, S., "On the coupling of wall-model immersed boundary conditions and curvilinear body-fitted grids for the simulation of complex geometries," *Computers & Fluids*, Vol. 226, 2021, p. 104996. https://doi.org/10.1016/j.compfluid.2021.104996.